Science
AAAS

Highly Crystalline Multimetallic Nanoframes with Three-Dimensional Electrocatalytic Surfaces

Chen Chen *et al.*

Science **343**, 1339 (2014);
DOI: 10.1126/science.1249061

Science (print ISSN 0036-8075; online ISSN 1095-9203) is published weekly, except the last week in December, by the American Association for the Advancement of Science, 1200 New York Avenue NW, Washington, DC 20005.

directions. At low T, in the present classical theory without randomness, $S_{\Phi x}$ vanishes as $T \to 0$; however, pinning of the charge order by impurities is likely responsible for the observed $S_{\Phi x}$ (*24*, *25*). At high T, our assumption of a T-independent bare ρ_s starts failing at $T \approx 2T_c$, and we expect a crossover to a theory with substantial amplitude fluctuations and smaller $S_{\Phi x}$ with increasing T.

Next, we examined the superconducting correlations by computing the associated helicity modulus (Fig. 4). This allows us to determine T_c by comparing against the expected universal jump (*26*). We find a T_c below the peak in $S_{\Phi x}$. This is consistent with the arguments in (*10*), which predicted a monotonic decrease in charge order through T_c: Evidently those computations only apply in a narrow window about T_c. We have not accounted for interlayer couplings in our two-dimensional theory: These can raise T_c and yield a cusplike singularity in the charge order at T_c.

One of the fundamental aspects of our theory is that the same set of parameters used above to describe x-ray scattering experiments also predict the strength of superconducting fluctuations above T_c. The latter are detectable in diamagnetism measurements, and indeed $YBa_2Cu_3O_{6+x}$ shows substantial fluctuation diamagnetism (*27*, *28*) over the range of temperatures that x-ray experiments measure charge-order fluctuations. We compute the diamagnetic susceptibility in the $N = \infty$ theory (*23*). Such a theory has effectively Gaussian superconducting fluctuations, albeit with a T dependence of the superconducting coherence length, which is different from the standard Landau-Ginzburg form (*29*). An absolute comparison of this theory with the observations (*28*) yields the value of a, which is found to differ by about 33% from the value obtained from the charge-order correlation length. Considering the simplicity of the $N = \infty$ theory, the possible differences in the x-ray and diamagnetism samples, and the absence of fitting to determine λ and w, this result is encouraging. For a sharper comparison, a Monte Carlo study of the crossover into a vortex-dominated regime (*30*–*32*) is needed. Eventually, with a complete study that also includes the effects of disorder and more detailed measurements of charge order and superconducting correlations on the same sample, we expect to be able to more tightly constrain the values of ga^2, wa^2, λ, and a.

Although we have only applied the theory to a doping where charge order is most pronounced, we argue that it is characteristic of the entire pseudogap phase. The dominant paradigms for the pseudogap have been phase-fluctuating superconductivity (*33*) and competing order (*12*, *13*), with experiments providing merit to both descriptions (*1*–*3*, *34*–*36*). This work unifies these paradigms in a single multicomponent order parameter that provides a natural description of the x-ray and diamagnetism data. Computations of the influence of fluctuating superconductivity on photoemission spectra (*37*) should now be extended to include all components of our order parameter. Our model is also linked to theories of metals with antiferromagnetic spin fluctuations (*16*, *17*): With decreasing doping, there is a zero-field quantum critical point to the onset of antiferromagnetic order (*38*), and this indicates that our present model will have to be extended to explicitly include spin fluctuations (*39*) to apply at such densities.

References and Notes

1. G. Ghiringhelli *et al.*, *Science* **337**, 821–825 (2012).
2. J. Chang *et al.*, *Nat. Phys.* **8**, 871–876 (2012).
3. A. J. Achkar *et al.*, *Phys. Rev. Lett.* **109**, 167001 (2012).
4. A. J. Achkar *et al.*, http://arxiv.org/abs/1312.6630.
5. Y. Endoh *et al.*, *Phys. Rev. B* **37**, 7443–7453 (1988).
6. B. Keimer *et al.*, *Phys. Rev. B* **46**, 14034–14053 (1992).
7. In La_2CuO_4, there is long-range antiferromagnetic order below 325 K, but this is entirely due to the interlayer exchange interactions.
8. S. Chakravarty, B. I. Halperin, D. R. Nelson, *Phys. Rev. Lett.* **60**, 1057–1060 (1988).
9. A. M. Polyakov, *Phys. Lett. B* **59**, 79–81 (1975).
10. S. Sachdev, E. Demler, *Phys. Rev. B* **69**, 144504 (2004).
11. O. Zachar, S. A. Kivelson, V. J. Emery, *Phys. Rev. B* **57**, 1422–1426 (1998).
12. E. W. Carlson, V. J. Emery, S. A. Kivelson, D. Orgad, in *The Physics of Superconductors Vol II: Superconductivity in Nanostructures, High-T_c and Novel Superconductors, Organic Superconductors*, K. H. Bennemann, J. B. Ketterson, Eds. (Springer, Berlin, 2004), pp. 275–452.
13. S. Sachdev, *Rev. Mod. Phys.* **75**, 913–932 (2003).
14. S. Sachdev, R. La Placa, *Phys. Rev. Lett.* **111**, 027202 (2013).
15. S. A. Kivelson, E. Fradkin, V. J. Emery, *Nature* **393**, 550–553 (1998).
16. M. A. Metlitski, S. Sachdev, *Phys. Rev. B* **82**, 075128 (2010).
17. K. B. Efetov, H. Meier, C. Pépin, *Nat. Phys.* **9**, 442–446 (2013).
18. H. Meier, M. Einenkel, C. Pépin, K. B. Efetov, *Phys. Rev. B* **88**, 020506(R) (2013).
19. I. Affleck, Z. Zou, T. Hsu, P. W. Anderson, *Phys. Rev. B* **38**, 745–747 (1988).
20. E. Dagotto, E. Fradkin, A. Moreo, *Phys. Rev. B* **38**, 2926–2929 (1988).
21. P. A. Lee, N. Nagaosa, X.-G. Wen, *Rev. Mod. Phys.* **78**, 17–85 (2006).
22. S.-C. Zhang, *Science* **275**, 1089–1096 (1997).
23. See supplementary materials on *Science* Online.
24. M. Le Tacon *et al.*, *Nat. Phys.* **10**, 52–58 (2014).
25. L. Nie, G. Tarjus, S. A. Kivelson, http://arxiv.org/abs/1311.5580.
26. D. R. Nelson, J. M. Kosterlitz, *Phys. Rev. Lett.* **39**, 1201–1205 (1977).
27. L. Li *et al.*, *Phys. Rev. B* **81**, 054510 (2010).
28. I. Kokanović, D. J. Hills, M. L. Sutherland, R. Liang, J. R. Cooper, *Phys. Rev. B* **88**, 060505(R) (2013).
29. A. Larkin, A. Varlamov, *Theory of Fluctuations in Superconductors* (Clarendon, Oxford, 2005).
30. V. Oganesyan, D. A. Huse, S. L. Sondhi, *Phys. Rev. B* **73**, 094503 (2006).
31. D. Podolsky, S. Raghu, A. Vishwanath, *Phys. Rev. Lett.* **99**, 117004 (2007).
32. K. Sarkar, S. Banerjee, S. Mukerjee, T. V. Ramakrishnan, http://arxiv.org/abs/1309.3776.
33. V. J. Emery, S. A. Kivelson, *Nature* **374**, 434–437 (1995).
34. J. Corson, R. Mallozzi, J. Orenstein, J. N. Eckstein, I. Bozovi, *Nature* **398**, 221 (1999).
35. Z. A. Xu, N. P. Ong, Y. Wang, T. Kakeshita, S. Uchida, *Nature* **406**, 486–488 (2000).
36. T. Wu *et al.*, *Nat. Commun.* **4**, 2113 (2013).
37. S. Banerjee, S. Zhang, M. Randeria, *Nat. Commun.* **4**, 1700 (2013).
38. T. Wu *et al.*, *Phys. Rev. B* **88**, 014511 (2013).
39. S. Blanco-Canosa *et al.*, *Phys. Rev. Lett.* **110**, 187001 (2013).

Acknowledgments: We thank A. Chubukov, A. Georges, M.-H. Julien, B. Keimer, S. Kivelson, J. Orenstein, and A. Yacoby for useful discussions. This research was supported by the NSF under grant DMR-1103860 and the Natural Sciences and Engineering Research Council of Canada. This research was also supported in part by Perimeter Institute for Theoretical Physics; research at Perimeter Institute is supported by the Government of Canada through Industry Canada and by the Province of Ontario through the Ministry of Research and Innovation. R.G.M. and S.S. acknowledge the John Templeton Foundation for support.

Supplementary Materials

www.sciencemag.org/content/343/6177/1336/suppl/DC1
Supplementary Text
References (*40*–*42*)

23 September 2013; accepted 21 February 2014
10.1126/science.1246310

Highly Crystalline Multimetallic Nanoframes with Three-Dimensional Electrocatalytic Surfaces

Chen Chen,[1,2,3]* Yijin Kang,[4]* Ziyang Huo,[1,2] Zhongwei Zhu,[1,2] Wenyu Huang,[1,2] Huolin L. Xin,[2] Joshua D. Snyder,[4] Dongguo Li,[4] Jeffrey A. Herron,[5] Manos Mavrikakis,[5] Miaofang Chi,[6] Karren L. More,[6] Yadong Li,[3] Nenad M. Markovic,[4] Gabor A. Somorjai,[1,2] Peidong Yang,[1,2,7,8]† Vojislav R. Stamenkovic[4]†

Control of structure at the atomic level can precisely and effectively tune catalytic properties of materials, enabling enhancement in both activity and durability. We synthesized a highly active and durable class of electrocatalysts by exploiting the structural evolution of platinum-nickel (Pt-Ni) bimetallic nanocrystals. The starting material, crystalline $PtNi_3$ polyhedra, transforms in solution by interior erosion into Pt_3Ni nanoframes with surfaces that offer three-dimensional molecular accessibility. The edges of the Pt-rich $PtNi_3$ polyhedra are maintained in the final Pt_3Ni nanoframes. Both the interior and exterior catalytic surfaces of this open-framework structure are composed of the nanosegregated Pt-skin structure, which exhibits enhanced oxygen reduction reaction (ORR) activity. The Pt_3Ni nanoframe catalysts achieved a factor of 36 enhancement in mass activity and a factor of 22 enhancement in specific activity, respectively, for this reaction (relative to state-of-the-art platinum-carbon catalysts) during prolonged exposure to reaction conditions.

Platinum (Pt) is a highly efficient electrocatalyst for both the cathodic oxygen reduction reaction (ORR) in fuel cells (and metal-air batteries) and the hydrogen evolution reaction (HER) in alkaline electrolyzers (*1*–*19*). However, the high cost and scarcity of Pt are key obstacles for its broad deployment in fuel cells and metal-air batteries for both stationary and portable

applications. Intense research efforts have been focused on developing high-performance electrocatalysts with minimal precious metal content and cost (*1*–*16*). Specifically, alloying Pt with non-noble metals can reduce the Pt content of electrocatalysts by increasing their intrinsic activity (*1*–*13*). We demonstrated that the formation of a nanosegregated Pt(111)-skin structure over a bulk single-crystal alloy with Pt_3Ni composition enhanced the ORR activity by two orders of magnitude (versus Pt/C catalysts) through altered electronic structure of Pt surface atoms (*1*). Although these materials cannot be easily integrated into electrochemical devices, their outstanding catalytic performance needs to be mimicked in nanoparticulate materials that offer high surface areas. Caged, hollow, or porous nanoparticles offer a promising approach for meeting these performance goals. The hollow interior diminishes the number of buried nonfunctional precious metal atoms, and their uncommon geometry provides a pathway for tailoring physical and chemical properties. They have thus attracted increasing interest in fields such as catalysis, biomedical materials, and electronics (*5*–*7*, *19*–*27*).

Hollow nanostructures have been prepared by template-directed protocol relying on the removal of microbeads or nanobeads, treatments based on the Kirkendall effect and the galvanic displacement reaction (*19*–*28*). Here, we present a novel class of electrocatalysts that exploit structural evolution of bimetallic nanoparticles; specifically, $PtNi_3$ solid polyhedra are transformed into hollow Pt_3Ni nanoframes with surfaces that have three-dimensional (3D) molecular accessibility. Controlled thermal treatment of the resulting nanoframes forms the desired Pt-skin surface structure (*1*, *9*). Synthesis of Pt_3Ni nanoframes can be readily scaled up to produce high-performance electrocatalysts at gram scale, and our protocol can be generalized toward the design of other multimetallic nanoframe systems.

We synthesized $PtNi_3$ polyhedra in oleylamine that had a uniform rhombic dodecahedron morphology and size (20.1 ± 1.9 nm), as observed along three representative zone axes (Fig. 1A, Fig. 2A, and figs. S1 and S2). The oleylamine-capped $PtNi_3$ polyhedra were dispersed in nonpolar solvents such as hexane and chloroform and kept under ambient conditions for 2 weeks, during which they transformed into Pt_3Ni nanoframes (fig. S3) with unchanged symmetry and size (Fig. 1, Fig. 2, and fig. S4). Increasing the solution temperature to 120°C decreased the time needed for this morphological evolution to 12 hours (fig. S5). These conditions were used to trace the entire structural and compositional evolution process at 2-hour time intervals (fig. S6). Samples at three representative stages (0, 6, and 12 hours) were examined by transmission electron microscopy (TEM) (Fig. 1, A to C). The initially solid nanostructures gradually eroded into hollow frames, and the bulk composition changed from $PtNi_3$ to PtNi and eventually Pt_3Ni, as evidenced by x-ray diffraction (XRD) patterns and energy-dispersive x-ray (EDX) spectra (fig. S7): All three samples are face-centered cubic (fcc), and the three main XRD peaks for each sample—(111), (200), and (220)—are located between those for Pt and Ni; during the evolution process, the peaks shifted toward lower angle (increased *d* spacing), which suggests that the nanostructures had changed from Ni-rich to Pt-rich alloys, in accordance with the EDX results. After dispersion of nanoframes onto a carbon support with high surface area (Vulcan XC-72) and subsequent thermal treatment in inert gas (Ar) atmosphere between 370° and 400°C, most nanoframes developed the smooth Pt-skin type of structure (Fig. 1D).

High-resolution TEM (HRTEM) showed that the initial $PtNi_3$ polyhedra were fcc nanocrystals (Fig. 2). For the hollow Pt_3Ni nanoframes, high-angle annular dark-field scanning TEM images showed an architecture consisting of 24 edges (width ~2 nm) of the parent rhombic dodecahedron (Fig. 2B) that maintained the single-crystalline structure (figs. S2 and S8).

In contrast to other synthesis procedures for hollow nanostructures that involve corrosion induced by harsh oxidizing agents or applied potential, the method described here proceeds spontaneously in air through free corrosion. We followed the compositional evolution of these framed, bimetallic nanostructures with x-ray photoelectron spectroscopy (XPS). In the presence of dissolved oxygen, the surface Ni atoms are more susceptible to oxidation than Pt atoms. The Ni 2p and Pt 4f XPS spectra of $PtNi_3$ polyhedra obtained in vacuum (Al Kα, $h\nu$ = 1486.6 eV) show that the majority of the surface Ni was oxidized and the surface Pt was mainly in the metallic state (Fig. 2, D and E). Oxidized Ni can readily form soluble metal complexes with the oleylamine ligands (*29*) and lead to a higher dissolution rate for Ni versus Pt that drives compositional change from Ni-rich to Pt-rich, until the stable Pt_3Ni phase (*30*) is formed. The intensity of Pt^{2+} with respect to Pt was barely altered after the system evolved into the final stage (Fig. 2, D and E), whereas the ratio of Ni^{x+} at the surface decreased substantially, implying that oxidation of Ni on the surface became more difficult in the stable Pt_3Ni composition. Additionally, we carried out in situ ambient-pressure XPS studies to examine the changes in surface chemistry of both $PtNi_3$ and Pt_3Ni in response to the different exposure atmospheres (*31*), the results of which support the mechanism proposed above (see fig. S10).

The corresponding morphological changes of the solid polyhedral particles occurred through

[1]Department of Chemistry, University of California, Berkeley, CA 94720, USA. [2]Materials Sciences Division, Lawrence Berkeley National Laboratory, Berkeley, CA 94720, USA. [3]Department of Chemistry, Tsinghua University, Beijing 100084, P. R. China. [4]Materials Science Division, Argonne National Laboratory, Argonne, IL 60439, USA. [5]Department of Chemical and Biological Engineering, University of Wisconsin, Madison, WI 53706, USA. [6]Division of Materials Science and Technology, Oak Ridge National Laboratory, Oak Ridge, TN 37831, USA. [7]Department of Chemistry, Faculty of Science, King Abdulaziz University, P.O. Box 80203, Jeddah 21589, Saudi Arabia. [8]Kavli Energy NanoSciences Institute at the University of California, Berkeley, and Lawrence Berkeley National Laboratory, Berkeley, CA 94704, USA.

*These authors contributed equally to this work.
†Corresponding author. E-mail: p_yang@berkeley.edu (P.Y.); vrstamenkovic@anl.gov (V.R.S.)

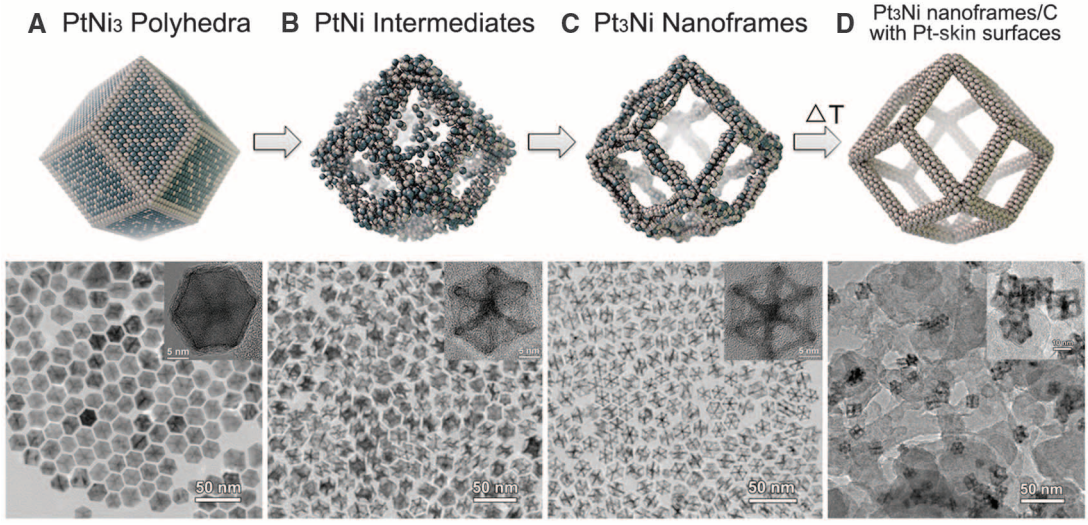

Fig. 1. Schematic illustrations and corresponding TEM images of the samples obtained at four representative stages during the evolution process from polyhedra to nanoframes. (**A**) Initial solid $PtNi_3$ polyhedra. (**B**) PtNi intermediates. (**C**) Final hollow Pt_3Ni nanoframes. (**D**) Annealed Pt_3Ni nanoframes with Pt(111)-skin–like surfaces dispersed on high–surface area carbon.

preferential dissolution in the interior of the polyhedral faces, rather than on the edges, driven by an inhomogeneous elemental distribution in the initial nanostructure revealed by TEM (Figs. 1 and 2). The contour of frames could be imaged immediately after synthesis because of the higher Pt content on the edges. EDX elemental mapping (Fig. 2C) and site-specific EDX analyses (fig. S11) for the $PtNi_3$ polyhedra showed that Ni exhibited a relatively homogeneous distribution inside of the particles, whereas Pt was relatively concentrated at the edges. Such elemental distribution in the original solid polyhedra could be caused by preferential etching of low-coordinated Ni along the edges because of the presence of trace oxygen in the solution during the initial nanoparticle synthesis. During the evolution process to form the nanoframes, this led to stable Pt_3Ni composition on the edges (Fig. 2C), as both Pt and Ni species were removed from the interior of the polyhedra (i.e., as Ni atoms were dissolved, Pt atoms were exfoliated from the Ni-rich interior). Together, the inhomogeneous distribution of Pt on the edges versus the interior and the high dissolution rate of Ni create hollow Pt_3Ni nanoframes containing 24 2-nm-thick edges that retain the high crystallinity of the parent structure (fig. S8).

The electrocatalytic properties of Pt_3Ni nanoframes were evaluated and compared to PtNi/C and commercial state-of-the-art Pt/C nanoscale electrocatalysts (Fig. 3). The polarization curves in Fig. 3B show an increase in ORR activity in the following order: Pt/C < PtNi/C << Pt_3Ni nanoframes. As seen in the Tafel plot (Fig. 3C), Pt_3Ni nanoframes exhibited substantially higher activity, with a slope of 46 mV dec^{-1} (versus 73 mV dec^{-1} for Pt/C), which is in agreement with that of Pt_3Ni (111)–Pt-skin (*3*). The kinetic current densities representing the intrinsic activities were calculated by the Koutecky-Levich equation and summarized in Fig. 3, E and F, as specific and mass activities, respectively. The specific activities were calculated through normalization by the electrochemically active surface area (ECSA) as estimated by CO stripping (electro-oxidation of adsorbed CO).

The ratio between ECSA values determined by integrated charge from CO stripping ($ECSA_{CO}$) and underpotentially deposited hydrogen ($ECSA_{Hupd}$)

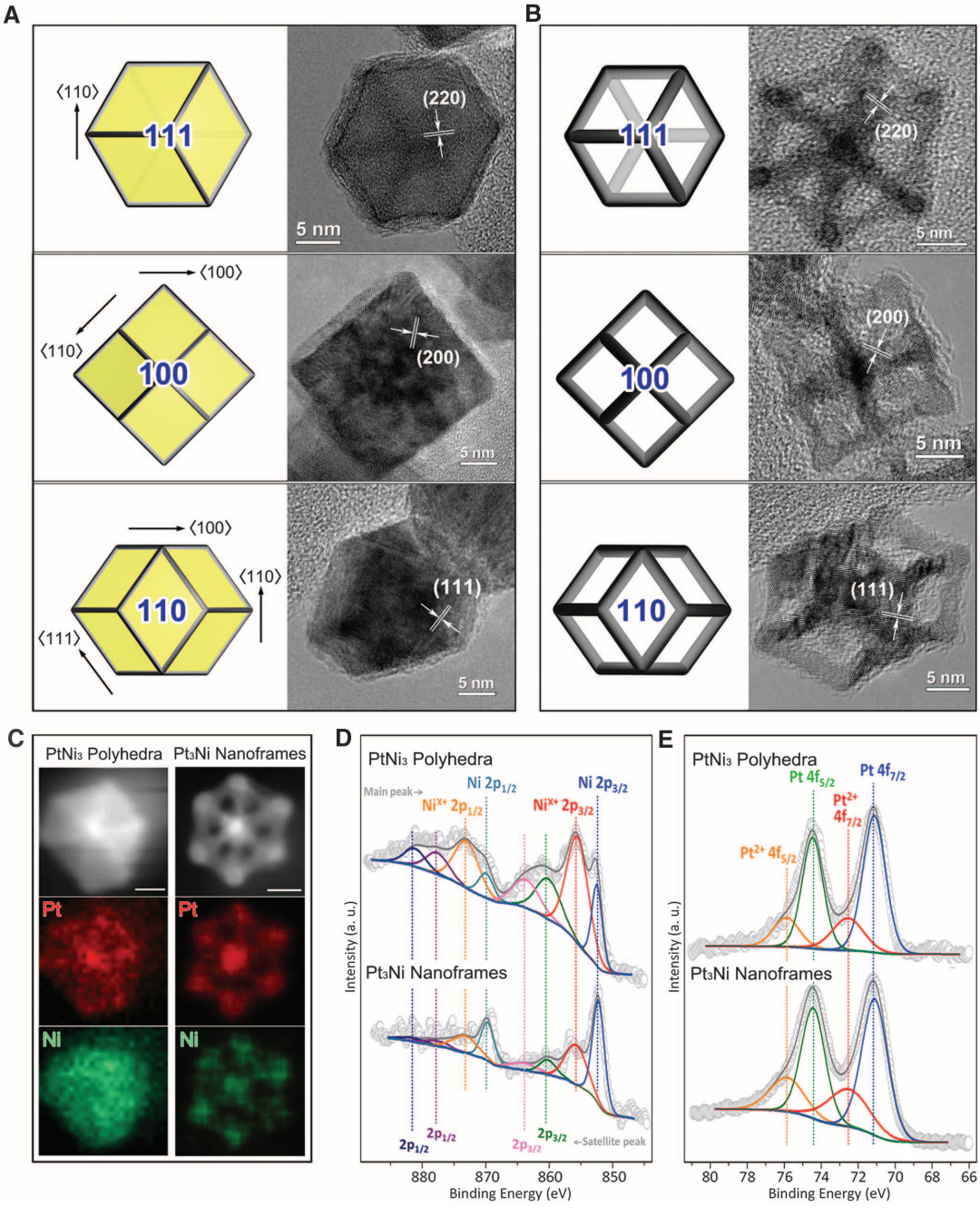

Fig. 2. Characterization of the initial $PtNi_3$ polyhedron and final Pt_3Ni nanoframes. (**A**) Three typical principle projections of the initial $PtNi_3$ polyhedron revealed a morphology of solid rhombic dodecahedron with single crystallinity. (**B**) The final Pt_3Ni nanoframe well inherits the symmetry and single crystallinity of parent $PtNi_3$ polyhedron, with a hollow interior developed and 24 edges (width ~2 nm) remaining. For each projection of both initial polyhedron and final nanoframe, the schematic illustration (left) and HRTEM image (right) are shown. (**C**) EDX elemental mapping results for $PtNi_3$ polyhedron and Pt_3Ni nanoframe, suggesting that Ni is homogeneously distributed whereas Pt in the parent $PtNi_3$ has a slightly higher ratio on the edges (scale bar, 5 nm). (**D**) Ni 2p and (**E**) Pt 4f XPS spectra of $PtNi_3$ polyhedra and Pt_3Ni nanoframes, from which it can be seen that, during the evolution process, the intensity of Ni^{x+} relative to Ni decreases whereas the relative ratio of Pt^{2+} to Pt is barely changed.

was 1.52 for the Pt_3Ni nanoframes, which strongly suggests the formation of a Pt-skin–terminated (111)-like surface structure (Fig. 3A and table S1) (*4*). Moreover, EDX line profiles confirmed the presence of Pt-skin on the nanoframe surfaces with a thickness of at least two Pt monolayers (MLs) (fig. S13). As a result, the specific activity of Pt_3Ni nanoframes at 0.95 V exhibited an improvement factor of >16 versus commercial Pt/C electrocatalyst (Fig. 3E). The extraordinarily high activity of the Pt_3Ni nanoframes, combined with the distinct $ECSA_{CO}/ECSA_{Hupd}$ ratio and EDX line profile, is indicative of a Pt_3Ni–Pt-skin formation, with a topmost Pt-skin thickness of at least 2 MLs rather than 1 ML, which is common for ideal bulk $Pt_3Ni(111)$ single crystal. Despite that divergence, 2 MLs of Pt-skin indeed sustain the enhancement in the ORR rate that is based on altered electronic structure of Pt topmost atoms by subsurface Ni, causing a lower surface coverage of spectator oxygenated species, namely OH_{ad}, and hence superior catalytic properties (*1*).

Surface strain of the Pt atoms also contributes to the functional properties of the nanoframes. The influence of strain on catalytic behavior was evaluated by density functional theory (DFT) simulations in which dependence of activity versus Pt-skin thickness was estimated to be optimal for 2 to 3 MLs (see fig. S15). These findings shed light on the origin of the high catalytic activity as well as the durability of the catalyst. The Pt-skin surface structure of the nanoframes in conjunction with their high ECSA provides the link between well-defined extended surfaces and highly crystalline nanoscale electrocatalysts. The synergy between specific activity and the open architecture of the Pt_3Ni nanoframes that enables access of reactants to both the internal and external surfaces (fig. S16) led to a factor of 22 enhancement in mass activity versus Pt/C catalysts (Fig. 3F). The mass activity calculated at 0.9 V (5.7 A mg^{-1} Pt) is more than an order of magnitude greater than the U.S. Department of Energy's 2017 target (0.44 A mg^{-1} Pt).

In addition to the high intrinsic and mass activities, the Pt_3Ni nanoframes exhibited remarkable durability throughout electrochemical operation. We cycled the potential between 0.6 and 1.0 V for a duration of 10,000 potential cycles at different sweep rates from 2 to 200 mV s^{-1}. For the state-of-the-art Pt/C electrocatalysts, such cycles cause substantial loss of specific surface area (~40%) because of dissolution of Pt surface atoms and agglomeration of Pt particles through surface oxidation/reduction processes (*8*, *18*). In contrast, STEM (dark-field and bright-field) images confirmed that the frame structure was preserved while activity loss was negligible after 10,000 potential cycles (Fig. 4). The enhanced durability is ascribed to the electronic structure of the Pt-skin surface resulting in a lower coverage of oxygenated intermediates because of the weaker oxygen binding strength, which diminishes the probability of Pt dissolution (*1*). In addition, the optimized Pt-skin thickness of at least 2 MLs hinders the loss of subsurface transition metal through the place-exchange mechanism during electrochemical operation, consequently preserving the high intrinsic activity (*9*). The Pt_3Ni nanoframe structure was retained after annealing at 400°C in Ar for several hours, demonstrating its thermal stability (fig. S19).

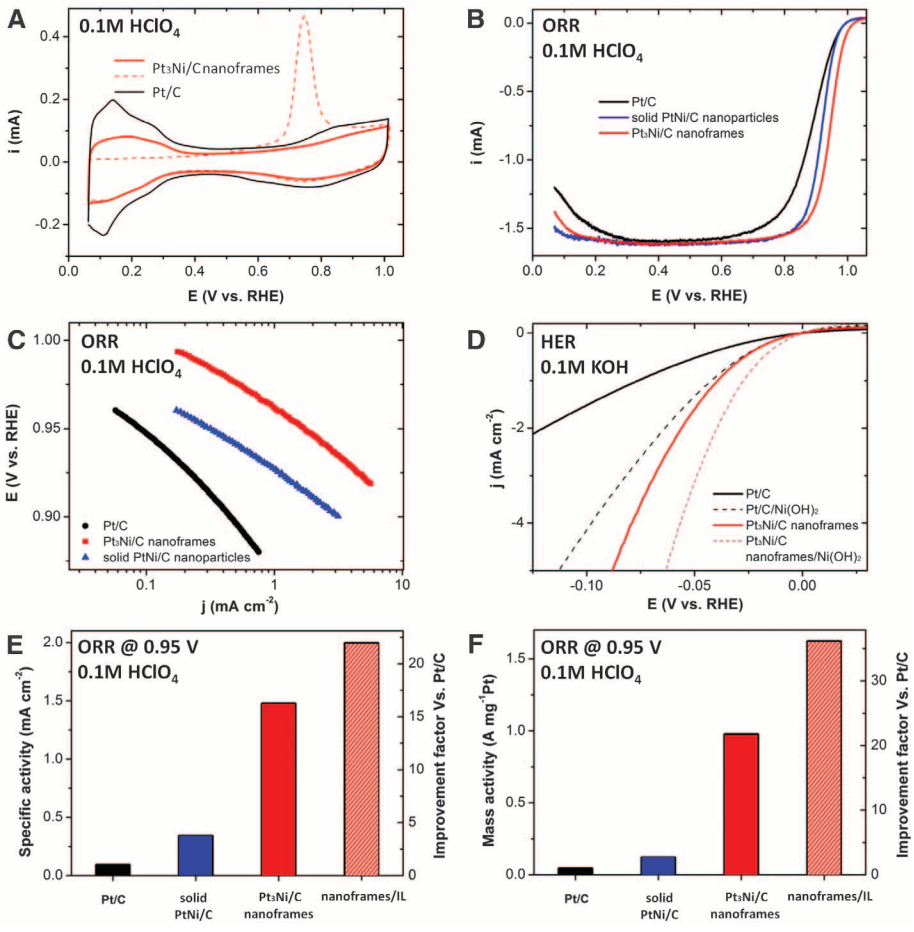

Fig. 3. Electrochemical properties of Pt_3Ni nanoframes. (**A**) Cyclic voltammograms of Pt/C and Pt_3Ni/C nanoframes signify the difference in surface coverage by H_{upd} and OH_{ad}. ECSA of the nanoframes is determined by integrated charge of adsorbed CO electro-oxidation curve. (**B**) ORR polarization curves. (**C**) The corresponding Tafel plots. (**D**) HER activities for Pt/C, $Pt/Ni(OH)_2$/C, Pt_3Ni nanoframes/C, and Pt_3Ni frames/$Ni(OH)_2$/C in alkaline electrolyte. (**E** and **F**) Specific activities (E) and mass activities (F) measured at 0.95 V, and improvement factors versus Pt/C catalysts. Because of the high intrinsic activity of the Pt_3Ni nanoframes, the ORR activity values are given at 0.95 V in order to avoid the extensive error margin at 0.9 V introduced by the close proximity of current values to the diffusion-limited current. IL, ionic liquid.

As reported by Erlebacher and co-workers, protic ionic liquids can be integrated into a nanoporous catalyst, where the high O_2 solubility of ionic liquids increases the O_2 concentration at the catalyst surface, resulting in higher attempt frequencies for the ORR and consequently higher activity (*5*, *6*). We used [MTBD][NTf_2] (fig. S20), an ionic liquid that has an O_2 solubility ($C_{O_2,[MTBD][NTf_2]}$ = 2.28 ± 0.12 mM) approximately twice that of the common electrolyte $HClO_4$ [$C_{O_2,HClO_4}$ = 1.21 mM (*6*); see supplementary materials]. Capillary forces exerted by the Pt_3Ni nanoframes pulled the ionic liquid inside the frames and prevented it from being washed away by electrolyte (Fig. 3A and figs. S21 to S23). The ionic liquid–encapsulated Pt_3Ni nanoframes showed sustained superior activity upon prolonged (10,000) potential cycling without noticeable decay in performance, providing further support for the frame architecture as a desired morphology to fully exploit the beneficial properties of ionic liquids (fig. S24). The ionic liquid–encapsulated Pt_3Ni nanoframes exhibited a factor of 36 enhancement in mass activity and a factor of 22 enhancement in specific activity relative to Pt/C catalysts.

We also applied these electrocatalysts to the HER, which is the crucial cathodic reaction in water-alkali electrolyzers. Electrochemically deposited $Ni(OH)_2$ clusters on Pt surfaces were recently shown to facilitate dissociation of water, thus increasing the HER activity (*14*). In the case of highly crystalline Pt_3Ni–Pt-skin nanoframe surfaces modified by electrochemically deposited $Ni(OH)_2$ clusters (Fig. 3D and fig. S25), the HER activity was enhanced by almost one order of magnitude relative to Pt/C. This result further

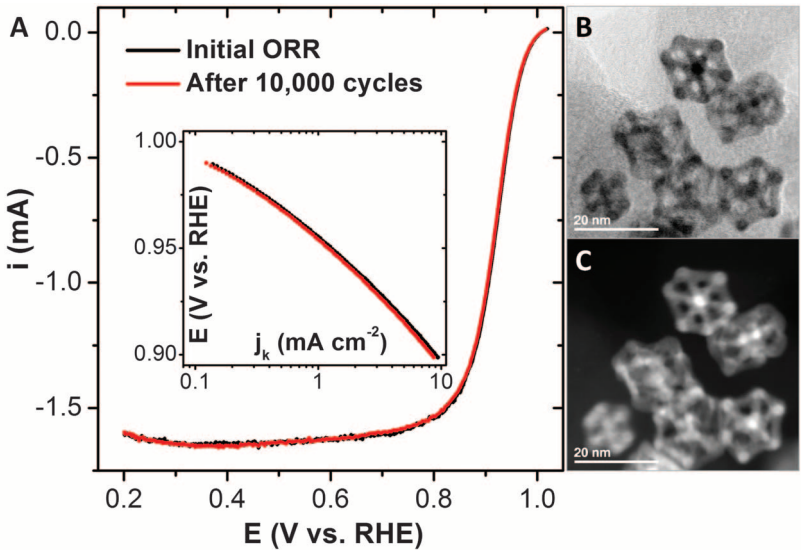

Fig. 4. Electrochemical durability of Pt_3Ni nanoframes. (**A**) ORR polarization curves and (inset) corresponding Tafel plots of Pt_3Ni frames before and after 10,000 potential cycles between 0.6 and 1.0 V. (**B** and **C**) Bright-field STEM image (B) and dark-field STEM image (C) of Pt_3Ni nanoframes/C after cycles.

emphasizes the beneficial effects of the open architecture and surface compositional profile of the Pt_3Ni nanoframes in electrocatalysis.

The open structure of the Pt_3Ni nanoframes addresses some of the major design criteria for advanced nanoscale electrocatalysts, namely, high surface-to-volume ratio, 3D surface molecular accessibility, and optimal use of precious metals. The approach presented here for the structural evolution of a bimetallic nanostructure from solid polyhedra to hollow highly crystalline nanoframes with controlled size, structure, and composition can be readily applied to other multimetallic electrocatalysts such as PtCo, PtCu, Pt/Rh-Ni, and Pt/Pd-Ni (figs. S26 to S29).

References and Notes

1. V. R. Stamenkovic *et al.*, *Science* **315**, 493–497 (2007).
2. S. Guo, S. Zhang, S. Sun, *Angew. Chem. Int. Ed.* **52**, 8526–8544 (2013).
3. D. F. van der Vliet *et al.*, *Nat. Mater.* **11**, 1051–1058 (2012).
4. D. F. van der Vliet *et al.*, *Angew. Chem. Int. Ed.* **51**, 3139–3142 (2012).
5. J. Snyder, K. Livi, J. Erlebacher, *Adv. Funct. Mater.* **23**, 5494–5501 (2013).
6. J. Snyder, T. Fujita, M. W. Chen, J. Erlebacher, *Nat. Mater.* **9**, 904–907 (2010).
7. J. Erlebacher, M. J. Aziz, A. Karma, N. Dimitrov, K. Sieradzki, *Nature* **410**, 450–453 (2001).
8. P. J. Ferreira *et al.*, *J. Electrochem. Soc.* **152**, A2256–A2271 (2005).
9. C. Wang *et al.*, *J. Am. Chem. Soc.* **133**, 14396–14403 (2011).
10. D. Wang *et al.*, *Nat. Mater.* **12**, 81–87 (2013).
11. J. Zhang, H. Yang, J. Fang, S. Zou, *Nano Lett.* **10**, 638–644 (2010).
12. C. Cui, L. Gan, M. Heggen, S. Rudi, P. Strasser, *Nat. Mater.* **12**, 765–771 (2013).
13. S.-I. Choi *et al.*, *Nano Lett.* **13**, 3420–3425 (2013).
14. R. Subbaraman *et al.*, *Science* **334**, 1256–1260 (2011).
15. Y. Liu, D. Gokcen, U. Bertocci, T. P. Moffat, *Science* **338**, 1327–1330 (2012).
16. Y. Kang *et al.*, *J. Am. Chem. Soc.* **135**, 2741–2747 (2013).
17. M. Cargnello *et al.*, *Science* **341**, 771–773 (2013).
18. L. Tang *et al.*, *J. Am. Chem. Soc.* **132**, 596–600 (2010).
19. Y. Yin *et al.*, *Science* **304**, 711–714 (2004).
20. J. E. Macdonald, M. Bar Sadan, L. Houben, I. Popov, U. Banin, *Nat. Mater.* **9**, 810–815 (2010).
21. S. E. Skrabalak *et al.*, *Acc. Chem. Res.* **41**, 1587–1595 (2008).
22. M. McEachran *et al.*, *J. Am. Chem. Soc.* **133**, 8066–8069 (2011).
23. J. X. Wang *et al.*, *J. Am. Chem. Soc.* **133**, 13551–13557 (2011).
24. M. E. Davis, *Nature* **417**, 813–821 (2002).
25. S. A. Johnson, P. J. Ollivier, T. E. Mallouk, *Science* **283**, 963–965 (1999).
26. M. S. Yavuz *et al.*, *Nat. Mater.* **8**, 935–939 (2009).
27. M. A. Mahmoud, W. Qian, M. A. El-Sayed, *Nano Lett.* **11**, 3285–3289 (2011).
28. M. H. Oh *et al.*, *Science* **340**, 964–968 (2013).
29. D. Wang, Y. Li, *Inorg. Chem.* **50**, 5196–5202 (2011).
30. C. E. Dahmani, M. C. Cadeville, J. M. Sanchez, J. L. Morán-López, *Phys. Rev. Lett.* **55**, 1208–1211 (1985).
31. F. Tao *et al.*, *Science* **322**, 932–934 (2008).

Acknowledgments: The research conducted at Lawrence Berkeley National Laboratory (LBNL) and Argonne National Laboratory (ANL) was supported by the U.S. Department of Energy (DOE), Office of Science, Office of Basic Energy Sciences (BES), Materials Sciences and Engineering Division, under contracts DE-AC02-05CH11231 and DE-AC02-06CH11357, respectively. The portion of work related to catalyst mass activity and durability was supported by the Office of Energy Efficiency and Renewable Energy, Fuel Cell Technologies Program. Work at the University of Wisconsin was supported by DOE, Office of Science, BES, under contract DE-FG02-05ER15731; computations were performed at supercomputing centers located at NERSC, PNNL, and ANL, all supported by DOE. We thank King Abdulaziz University for support of the Pt-Co bimetallic nanocatalyst work. Microscopy studies were accomplished at the Electron Microscopy Center at ANL, National Center for Electron Microscopy and Molecular Foundry at LBNL, and the Center for Nanophase Materials Sciences at Oak Ridge National Laboratory, which is sponsored by the Scientific User Facilities Division, BES, DOE. XPS studies were carried out at Advanced Light Source (LBNL). We thank S. Alayoglu for carrying out the site-specific EDX on the alloy nanostructures, H. Zheng for her help on TEM work at LBNL, and Z. Liu for help on XPS analysis.

Supplementary Materials

www.sciencemag.org/content/343/6177/1339/suppl/DC1
Materials and Methods
Figs. S1 to S30
Table S1
Movies S1 and S2
References (*32*–*38*)

27 November 2013; accepted 14 February 2014
Published online 27 February 2014;
10.1126/science.1249061

The Source Crater of Martian Shergottite Meteorites

Stephanie C. Werner,[1]* Anouck Ody,[2] François Poulet[3]

Absolute ages for planetary surfaces are often inferred by crater densities and only indirectly constrained by the ages of meteorites. We show that the <5 million-year-old and 55-km-wide Mojave Crater on Mars is the ejection source for the meteorites classified as shergottites. Shergottites and this crater are linked by their coinciding meteorite ejection ages and the crater formation age and by mineralogical constraints. Because Mojave formed on 4.3 billion–year-old terrain, the original crystallization ages of shergottites are old, as inferred by Pb-Pb isotope ratios, and the much-quoted shergottite ages of <600 million years are due to resetting. Thus, the cratering-based age determination method for Mars is now calibrated in situ, and it shifts the absolute age of the oldest terrains on Mars backward by 200 million years.

The martian rock collection contains nearly 150 meteorite specimens: shergottites, nakhlites, and chassignites, as well as one orthopyroxenite (ALH84001) (*1*, *2*). Currently, the oldest rock linked to Mars appears to be ALH84001, crystallized about 4.1 billion years ago (Ga) (*3*, *4*) and probably ejected from Mars 20 million years ago (Ma) (*5*). The original rock unit from which chassignites and nakhlites were ejected about 11 Ma (*5*) probably crystallized around 1.3 Ga (*1*, *2*, *6*). The apparent crystallization ages of shergottites are more diverse and range between 150 and 596 Ma (*1*, *2*, *6*, *7*). The geochemically depleted [in incompatible elements such as light rare earth elements (LREE) relative to the martian mantle (*8*)] shergottites cluster at the old age range, whereas the enriched

[1]The Centre for Earth Evolution and Dynamics, University of Oslo, Sem Sælandsvei 24, 0371 Oslo, Norway. [2]Laboratoire de Géologie de Lyon: Terre, Planètes, Environnement, Université de Lyon 1 (CNRS, ENS-Lyon, Université de Lyon), rue Raphaël Dubois 2, 69622 Villeurbanne, France. [3]Institut d'Astrophysique Spatiale, Université Paris Sud 11, Bâtiment 121, 91405 Orsay, France.

*Corresponding author. E-mail: stephanie.werner@geo.uio.no